HHS Public Access

Author manuscript

Cell Signal. Author manuscript; available in PMC 2016 July 01.

Published in final edited form as:

Cell Signal. 2015 July ; 27(7): 1413–1425. doi:10.1016/j.cellsig.2015.03.024.

Mixed-Effects Model of Epithelial-Mesenchymal Transition Reveals Rewiring of Signaling Networks

Poonam Desai[1], **Jun Yang**[2], **Bing Tian**[2,3], **Hong Sun**[2], **Mridul Kalita**[3], **Hyunsu Ju**[2,4,5], **Adriana Paulucci-Holthauzen**[6], **Yingxin Zhao**[2,3,4], **Allan R. Brasier**[2,3,4], and **Rovshan G. Sadygov**[1,3,*]

[1]Department of Biochemistry and Molecular Biology, University of Texas Medical Branch, Galveston, TX 77555

[2]Department of Internal Medicine, University of Texas Medical Branch, Galveston, TX 77555

[3]Sealy Center for Molecular Medicine, University of Texas Medical Branch, Galveston, TX 77555

[4]Institute for Translational Sciences, University of Texas Medical Branch, Galveston, TX 77555

[5]Department of Preventive Medicine and Community Health, University of Texas Medical Branch, Galveston, TX 77555

[6]Optical Microscopy Core, University of Texas Medical Branch, Galveston, TX 77555

Abstract

The type II Epithelial-Mesenchymal Transition (EMT) produces airway fibrosis and remodeling, contributing to the severity of asthma and chronic obstructive pulmonary disease. While numerous studies have been done on the mechanisms of the transition itself, few studies have investigated the system effects of EMT on signaling networks. Here, we use mixed effects modeling to develop a computational model of phospho-protein signaling data that compares human small airway epithelial cells (hSAECs) with their EMT-transformed counterparts across a series of perturbations with 8 ligands and 5 inhibitors, revealing previously uncharacterized changes in signaling in the EMT state. Strong couplings between Menadione, TNFα and TGFβ and their known phospho-substrates were revealed after mixed effects modeling. Interestingly, the overall phospho-protein response was attenuated in EMT, with loss of Mena and TNFα coupling to heat shock protein

*Corresponding Author: Rovshan Sadygov, rovshan.sadygov@utmb.edu.

Author Contributions

The lead investigators for this project were Rovshan Sadygov (computational) and Allan Brasier (experimental). Allan Brasier conceived the idea, designed, and carried out the experiments. Bing Tian designed and carried out initial perturbation experiments and cellular staining. Jun Yang carried out initial perturbation experiments, and designed and conducted the validation experiments. Hong Sun performed phospho-proteomic assays. Mridul Kalita performed data collection and analysis. Adriana Paulucci conducted the confocal microscopy, and z stacking reconstruction. Yingxin Zhao validated HSP27 dysregulation and aided in data interpretation. Rovshan Sadygov developed the mixed-effects model. Poonam Desai developed the mixed-effects model and generated Cytoscape figures. Hyunsu Ju aided in the discussion of the results. All authors contributed to the writing of the manuscript.

Conflict of Interest Statement: The authors declare that they have no conflict of interest.

(HSP)-27. These differences persisted after correction for EMT-induced changes in phospho-protein substrate abundance. Construction of network topology maps showed significant changes between the two cellular states, including a linkage between glycogen synthase kinase (GSK)-3α and small body size/ Mothers Against Decapentaplegic (SMAD)2. The model also predicted a loss of p38 mitogen activated protein kinase (p38MAPK)-independent HSP27 signaling, which we experimentally validated. We further characterized the relationship between HSP27 and signal transducers and activators of transcription (STAT)3 signaling, and determined that loss of HSP27 following EMT is only partially responsible for the downregulation of STAT3. These rewired connections represent therapeutic targets that could potentially reverse EMT and restore a normal phenotype to the respiratory mucosa.

Keywords

Mixed-effects modeling; EMT; cellular signaling; correlative networks

1 INTRODUCTION

The respiratory tract is lined by a mucosal barrier consisting of relatively impermeable epithelial sheet connected by tight junctions that restrict fluid loss and limit inhaled particulate access to the internal milieu[1]. Maintenance of epithelial integrity is critical to normal cellular signaling, pulmonary homeostasis, and response to toxicants and allergen exposures. Moreover, this cell type plays a dynamic role in initiating innate signaling programs in response to physical, chemical and biological challenge through coordinating secretion of cytokines, defensins, and alarmins [2;3]. Injury, subsequent inflammation and the loss of epithelial basement membrane integrity also promote epithelial cell activation by extracellular matrix-associated factors. These resident growth factors include the transforming growth factor (TGF)β[2;4], one of the primary pathways involved in epithelial repair.

TGFβ binds to the extracellular transmembrane serine, threonine kinase TGFβ receptor type II (TGFβRII) that recruits and phosphorylates TGFβRI to signal through Smad-dependent, “canonical” and Smad-independent “noncanonical” pathways[5;6]. In the canonical pathway, phosphorylated Smad2/3 binds to Smad4 and the complex then translocates to the nucleus. The noncanonical signaling pathways involve downstream PI3K/Akt, Ras small GTPases, Wnt/β-catenin, ERK, p38MAPK, and JNK. Collectively, the canonical and noncanonical pathways converge on a core set of transcriptional repressors that function to initiate and maintain EMT. These include SNAIL (SNAI)1/2, zinc finger E-box binding (ZEB)1/2, Twist 1/2, and others [5;7].

TGFβ stimulates epithelial cells to become motile, fibroblast-like cells; this process is referred to as type II EMT[8], a response central to repair after tissue injury. TGFβ-induced type II EMT leads to disruption of mucosal barrier function by inducing the loss of apical polarity, reduced epithelial cadherin (ECad) and disruption of epithelial adherens junctions[6;8;9]. In addition, type II EMT enables transformed epithelial cells to express α-smooth muscle actin (SMA), stress fibers and intermediate filament vimentin, to produce

extra-cellular matrix through secretion of collagen and fibronectin, and to increase expression of matrix metalloproteinases to promote airway remodeling (Figure 1 A). Recently we have found that EMT also produces complex alterations in the tumor necrosis factor (TNF)α, signal transduction pathway [10]. The EMT state produces profound changes in TNFα signaling pathway coupling its canonical and noncanonical arms through transcriptional reprogramming of the TRAF1 and NFκB1 promoters [3;10]. As a result, the "coupling constant" e.g., the lag time between activation of the canonical and the noncanonical NF-κB program, was markedly reduced by EMT.

Due to the complexity of interacting signals and consequent global transcriptional reprogramming, systems-level studies are needed to fully understand how critical phosphorylation pathways affected by EMT. The "systems" concept relies on quantitative high throughput proteome measurements in response to external perturbation. This approach makes no *a priori* assumptions about the mechanisms underlying the response, allowing for the identification of new and less expected findings[3]. In this study, we develop a systems-level approach by perturbation of signaling programs in normal and EMT states followed by measurement of phospho-protein changes using enzyme-linked immunosorbent assays (ELISA) with bead-based microspheres[11]. To study effects induced by cell signaling, cells are stimulated using, for example, cytokines, and abundance of phospho-proteins measured. Stimulus-induced changes are then used to deduce which proteins are involved in specific signaling pathways and potentially causative effects of genes [12–14].

When doing such experiments, errors introduced by random effects (variability due to operators, day, wells - referred to as batch effects) can significantly affect the output values. Batch effects have been shown to be strong enough to alter the correlations between gene pairs. Normalization of data can remove this variance and reveal the true relationships between the biological variables of interest [12;15]. In this study, we evaluate the application of linear mixed-effects modeling to phospho-protein data from cells in the normal and EMT states in order to view the effects due purely to ligand stimulation. Mixed-effects modeling is a normalization method that can be used to separate fixed-effects parameters (the variables of interest) from the random effects.

In this study, we had two goals. First, we sought to determine the changes (rewiring) in the signaling pathways that occur due to the EMT. Our second purpose was to find out if any of the cellular interventions (cell treatments with kinase inhibitors) reveal "hidden" connections between phospho-proteins which are below the detection limits in a normal cell state, but become prominent under a series of perturbations. To accomplish these goals, we used the cells treated with several kinase inhibitors and stimulated them by several multiple ligands. The experimental design resulted in a large number of unique conditions, corresponding to each inhibitor and stimulant pair. Under these conditions, we interrogated the cells for 13 phospho-proteins using ELISA. The data was generated by several operators and in multiple experiments, and normalized by mixed-effects modeling. The normalized data aligned well with known canonical pathways in normal cells. It was used in correlative analysis to determine a connectivity network among the phospho-proteins. We found that the network was significantly rewired in the EMT state, a pattern that persisted after correcting for EMT-induced changes in the abundance of 4 phospho-proteins. This

experimental design also allowed the determination of the correlation effects between the stimulants and conditions. In addition, we have observed that intervention by a kinase inhibitor is able to reveal a non-conical origin of a heat shock protein phosphorylation. We experimentally validated the novel prediction that EMT rewires p38MAPK-independent HSP27 phosphorylation.

2 Methods

2.1 Cell culture and treatment

An immortalized human small airway epithelial cell (hSAEC) line was established by infecting primary hSAECs with human telomerase (hTERT) and cyclin dependent kinase (CDK)-4 retrovirus constructs and selecting under 250 ng/ml puromycin and 30 μg/ml G418 as previously described [16]. The immortalized hSAECs were grown in small airway epithelial cell growth medium (SAGM, Lonza, Walkersville, MD) in a humidified atmosphere of 5% CO_2. For induction of EMT, hSAECs were stimulated for 15 days with TGFβ (10 ng/ml, PeproTech Rocky Hill, NJ). For the conduct of the stimulation matrix, cells were plated into 12 well plates.

2.2 Immunostaining and Confocal Immunofluorescence Microscopy

For confocal fluorescence microscopy, 25-mm round microscope cover glasses (Fisher) were precoated with collagen solution (Roche Applied Science) in a culture plate. hSAECs or EMT-hSAECs were plated 1 day prior to the experiment. The cells were fixed with 4% paraformaldehyde in PBS and incubated with 0.1 m ammonium chloride for 10 min. Cells were permeabilized with 0.5% Triton-100, followed by incubation in blocking buffer (5% goat serum, 0.1% IGEPAL CA-630, 0.05% NaN3, and 1% BSA) and incubated with anti-Vimentin antibody (Santa Cruz Biotechnology, Inc) or Alexa-labeled phalloidin in incubation buffer (0.1% IGEPAL CA-630, 0.05% NaN3, and 2% BSA) overnight at 4 °C. After washing, cells were stained with Alexa Fluor 555-conjugated goat anti-rabbit IgG (Invitrogen) in incubation buffer for 1 h. Nuclei were stained with DAPI as previously[10;17].

2.3 Image collection and analysis

Images were collected using a Zeiss LSM-510 META confocal microscope with a 63X, 1.2 numerical aperture, water immersion objective, (Optical Microscopy Core at UTMB). The images were obtained using excitation lines at 364 nm (pseudo colored in blue), 543 nm (pseudo colored in red), 633 nm (pseudo colored in green) and three different channels of emission with sequential acquisition. After excitation with the 364 nm laser line, emission was collected with a 385–470 nm filter, after excitation with the 543 laser line, emission was collected with a 560–615 nm filter and after excitation with 633nm laser line emission was collected with a LP650nm filter. Images were acquired with a optical zoom of 0.7, pixel size of 0.390 mm, pixel time of 2.51msec. Z-stack was acquired with z-slices of 0.8 mm. Images were processed and analyzed using Metamorph software and 3D rendering was performed using Imaris software. Relative fluorescence intensity for red and green channel was calculated for the cells body volume in the entire field of view and then normalized by the

number of cell counted based on DAPI nuclei staining, yielding the relative fluorescence intensity per cell. A total of 3 field of view per condition was analyzed and then averaged.

2.4 Experimental Design of Phospho-protein Signaling Experiment

To remove day-to-day variability, all cell stimulations were conducted on the same day by four different operators. 15 minutes prior to harvest, cells were treated with a ligand. Controls were not treated. The harvest protocols were standardized (buffers used, etc.). Following harvest, the extracts were frozen down. Each operator performed the experiment for two ligands (unreplicated), as well as a control (no ligand), under all inhibitor conditions. Thus, there were a total of eight no-ligand data points for every inhibitor. Activating ligands used were TNFα (20 ng/ml, Pepro-Tech), Insulin-like Growth Factor β (IGFβ, 10ng/ml, Peprotech), TGFβ (10 ng/ml, PeproTech), Interferon β (IFNβ, 2000 U/ml), Interleukin 6 (IL-6, 100 ng/ml, PeproTech), menadione (Mena, 20 μM, Sigma Aldrich), E. coli lipopolysaccharide (LPS, 50 μg/ml, Sigma Aldrich), and Polyinosinic:polycytidylic acid (PolyIC) (50 μg/ml, Sigma Aldrich).

Inhibitors, concentration used and kinase targets included: BMS345541 (50 μM, Sigma-Aldrich), an inhibitor of the IκB-kinase [18], iIKK; PD325901 (100 nM, Sigma-Aldrich) a Mitogen/ERK kinase inhibitor [19], iMEK; AG490 (100 μM, Calbiochem, EMD-Millipore), a janus kinase inhibitor, iJAK; OCID 5005 (20 μM, Orchid Research laboratories), a signal transducer and activator of transcription 3 inhibitor, iSTAT3; KU-55933 (10 μM Abcam), an inhibitor of ataxia-telangiectasia mutated [20], iATM.

2.5 Multiplex phospho-protein measurements

Luminex xMAP multiplex assays were conducted for phospho-Ser32/36-IκBα (pIκBα), phospho-Ser536-RelA (pp65), phospho-Thr180/Tyr182-P38 (pp38MAPK), phospho-Ser473-AKT (pAkt), phospho-Thr202/Tyr204, Thr185/Tyr187-ERK1/2 (pERK1/2), phospho-Ser21/Ser9-GSK3α (pGSK3α), phospho-Tyr-705-STAT3 (pSTAT3), phospho-Ser15-P53 (pp53), phospho-Ser380-P90-RSK (pp90RSK), phospho-Thr71-ATF2 (pATF2), phospho-Ser133-CREB (pCREB), phospho-Ser456/Ser467 SMAD2 (pSMAD2) and phospho-Ser78-HSP27 (pHSP27) according to the manufacturer's recommendations (Bioplex, Bio-Rad, Hercules, CA). For each plate a positive control cell lysate was used. A blank well was used to estimate background. Fluorescence intensity measurements were used for mixed-effects model development.

2.6 Mixed Effects Modeling

The data is processed in a single global model [12]. The experimental design was such that the ligands were nested with respect to the operators, and the controls (no ligand stimulation) were fully crossed (Figure E1, Supplementary Materials), thus it is possible to compare results across operators. The formula for the mixed-effects model is:

$$y_{vwxyz}=\mu+\ell_v+k_w+(\ell k)_{vw}+i_x+(ki)_{wx}+E_y+(kE)_{wy}+\delta_z+\varepsilon_{vwxyz} \quad (1)$$

where, y_{vwxyz} are the log10 transformed fluorescence intensities (FI), ℓ_v is the ligand factor, k_w is the kit (phospho-protein) factor, i_x is the inhibitor factor, E_y is the cell state factor, δ_z is

the operator random variable and ε_{vwxyz} is the technical error. μ is the grand mean of all pAKT measurements in hSAECs ($E_y = 0$) from all operators under the no stimuli, $\ell_v = 0$, and no inhibitor, $i_x = 0$ condition. The interaction terms between the factors are denoted in parenthesis. The effects of all remaining terms are computed relative to μ. For example, to compute levels of pp65 under EMT condition (EMT-hSAECs) from the cells stimulated by TGFβ and treated with iIKK, we will add to μ the effects due to the ligand, ℓ_v = TGFβ, ligand-protein interaction (TGFβ and pp65), $(\ell k)_{vw}$, the effect of the inhibitor, i_x = iIKK, the overall effect of EMT (E_y=1), and EMT:pp65 interaction term. The model, Eq. (1), has two variance components: one due to the operator random effect, δ_z, and the other due to the measurement error, ε_{vwxyz}. The operator effect has four levels (the number of operators in this study) and is modeled to affect the intercept, μ, only. Additional explanations to the terms in Eq. (1) are provided in Table E1 (Supplementary Materials).

The mixed-effects model can also be written to explicitly show the fixed effects (factors) and random effects:

$$y = X\beta + Zb + \varepsilon \quad (2)$$

where y is a vector of the observations, and b and are assumed to be normally (N) distributed:

$$\varepsilon \sim N(0, \sigma^2), b \sim N(0, \sigma_a^2), E[y] = X\beta \quad (3)$$

X and Z are the binary fixed effects (corresponding to a presence or absence of a specific treatment) and random effects (determined by the presence or absence of the random effect) design matrices, respectively. β is the fixed (treatment) effects vector, b is the random effects vector, and ε is the random variable describing measurement errors. X and Z relate the observations, y, to β and b, respectively. σ^2 is the variance component due to the experimental errors and σ_a^2 is the random effects.

2.7 Random Effects

Mixed-effects models provide separate estimates for the fixed effects and random effects. For the fixed effects, the model estimates their effect size (best linear unbiased estimates) with relevant coefficients, and standard errors. For the random effects, the model estimates the variance (σ_a^2 in Eqs (2) and (3)) of the population (of operators) from which the random effects term was drawn. The model provides the "estimates" of the random effects, known as the best linear unbiased predictor (BLUP). BLUP estimates, b_z, are smaller than the actual size, $(\overline{y_{...z}} - \overline{\overline{y}})$, of a random effect:

$$b_z = \frac{(\overline{y_{...z}} - \overline{\overline{y}})\,\sigma_a^2}{\sigma_a^2 + \frac{\sigma^2}{n_z}} \quad (4)$$

where, $\overline{y_{...z}}$ is the average of all observations, y, for the z^{th} operator, $\overline{\overline{y}}$ is the grand mean, and n_z is the number of measurements made by the z^{th} operator. We used the BLUP estimates in the normalization procedure.

2.8 Data Normalization and Visualization

The data is normalized to remove the operator effects (Eq. 4), using the equation:

$$y^*_{vwxyz} = \mu + \ell_v + (\ell k)_{vw} + i_x + (ki)_{wx} + \mathrm{E}_y + (\mathrm{E}k)_{wy} \quad (5)$$

Following normalization, the residuals (the difference between the observations and model fit in Eq. (1), ε_{vwxyz}) are added to the processed data, y^*_{vwxyz}, and the resulting data is back transformed (raised to the power of 10) to obtain the normalized FI:

$$FI^{norm} = 10^{(y^*_{vwxyz} + \varepsilon_{vwxyz})}$$

In the paper we refer to this data as the normalized data. In contrast, the original fluorescence intensities are referred to as the raw data.

The mixed-effects model was fit using the "lme4" package (version 1.1–5) [21] in R (version 3.1.0) [22]. lme4 fits the model using restricted maximum likelihood criterion (REML). The computed REML of the model was initially −201.8; however, we removed the largest outlier point resulting in a significant reduction of the REML to −298.8. For model fitting, this data point was added back. Plots and additional analyses were performed using R, and all network diagrams were created using the visualization software Cytoscape [23], with connection significance determined using correlations. To visualize the fixed effects due to the stimuli, network diagrams were created in Cytoscape, with the edges representing the fluorescence intensity differences between 0 (no stimuli) and 15 minutes (ligand stimulated cells) for each ligand-phospho-protein pair under a single inhibitor. For each edge,

$$width = \left(FI^{norm}_{t=15} - \frac{1}{8} \sum\nolimits_{\forall t=0} FI^{norm} \right) / 1000 \quad (6)$$

The eight phospho-protein measurements taken at t=0 are averaged, as there is no ligand being applied to cells at this time, and as such, the cells should all be under equal conditions. The red and green colors in the Cytoscape plots indicate decrease and increase, respectively, in a phospho-protein level. We used Eq. (6) with the raw (unprocessed) data as well. The FI values are divided by 1000, in order to allow Cytoscape to parse them. Figure 4 was made using the DataRail program [24].

2.9 Correlation Analysis

We constructed phospho-protein vectors consisting of 54 elements, corresponding to the combinations of the nine stimulus conditions (8 stimuli + 1 control) and six inhibitor conditions (5 inhibitors +1 control), resulting in a data matrix A, $A \in R^{mxn}$ where m=13 (number of phospho-proteins), and n=54 (number of conditions). There were two phospho-protein matrices A, one for hSAECs and one for EMT-hSAECs. The total number of data points was 2,496.

Correlations were calculated in R, using Pearson's product moment correlation coefficient. The significance of the correlation was based upon calculated p-values, using the cor.test()

function. The p-values were adjusted for multiple hypothesis testing using the Benjamini-Hochberg procedure [25] to control for false discovery rates. Partial correlations [26] were calculated between two phospho-proteins, while controlling for the effect of a third phospho-protein using the pcor.test() function of the "ppcor" R package. Partial correlations were only calculated for connections that were found to be significant in the initial correlation analysis.

2.10 HSP27 Transfection and Flow Cytometry

The human Hsp27 expression plasmid (pEGFP-hsp27, a gift from Andrea Doseff[27], Addgene plasmid # 17444) was transfected into EMT-hSAECs by electroporation using the Basic Epithelial Cells Nucleofector kit (Cat. # VPI-1005) on a Nucleofector II device running programme W-001 (Amaxa Biosystems, Lonza). Three days later, the cultured hSAECs, after 15 minutes of IL-6 stimulation at 100ng/ml, were harvested with trypsin and fixed immediately by adding an equal volume of IC Fixation buffer (eBioscience) for 30 minutes at room temperature. The cells were then resuspended in 1ml 100% methanol and incubated at 4°C for at least 30 minutes. After incubation, the cells were washed 3 times in FACS buffer and stained with Alexa Fluor 647-conjugated anti-phospho-STAT3 (Tyr705) antibody (Cat. #4324, Cell Signaling) according to the manufacture's instruction. Samples were measured by FACSCanto (BD Biosciences) and data were analyzed with FlowJo software.

3 Results

3.1 Phospho-protein Signaling Experiment

Normal primary small airway epithelial cells (hSAECs) isolated from the bronchiole are cuboidal cells that grow in polarized monolayers. Normally, the intracellular distribution of polymerized actin filaments are found in low abundance in the periphery of the cell revealed by phalloidin staining (Figure 1B, top left panel). Similarly, hSAECs express low amounts of vimentin that appear in disorganized perinuclear caps (Figure 1B, top middle and right panels). By contrast, EMT-hSAECs show distinct distribution of polymerized actin in bundles characteristic of intracellular stress-fibers (Figure 1B, bottom left panel). A marked induction of mesenchymal vimentin is seen, associated with organized assembly into structured intermediate filaments (Figure 1B, bottom middle and right panels). Quantification of total vimentin expression reveals a 5-fold increase in its expression after the mesenchymal transition (Figure 1B).

These distinct morphological features are not only caused by changes in signaling, but must be maintained by specific signaling programs as well. To obtain functional information on how EMT affects phospho-protein signaling networks, we conducted experiments on hSAECs and EMT-hSAECs stimulated by eight different ligands in the absence or presence of five small molecule inhibitors (Figure 1C, Methods). These ligands were selected to broadly activate plasma membrane toll-like and death domain receptors, and primary pattern recognition receptors of the innate signaling pathways. The inhibitors were selected to affect primary known signaling kinases based on current experimental information, and concentrations were adjusted to achieve >90% inhibition of its major target. The thirteen

phospho-proteins measured were chosen to represent canonical signaling pathways that are involved in the process of EMT (Figure 1A, 1C).

This high-throughput data was organized in a set of arrays based upon the different states of proteins under multiple conditions, over multiple experiments performed by four different operators on the same day, in order to minimize between-day variance (Figure 1D). In total, the data consists of 2,496 points, with 192 points for each phospho-protein, as each operator performed experiments for two ligands, along with a control measurement taken with each ligand, to yield 8 control replicates (Figure E1).

In order to accurately deconstruct the effects of treatment, and to account for random effect due to differences in experimental operator, we used a linear mixed-effects model to normalize the data. The model calculates the individual effect of each variable on phosphorylation (Methods, Equation 1), and sums these terms to yield the fitted data. The fixed effects terms represented the ligands, inhibitors, phospho-proteins, and EMT state. The technical error was accounted for by Gaussian noise. The model computes the effects of all the terms relative to μ, the grand mean of all pAKT measurements in hSAECs from all operators under the condition of no stimulus and no inhibitor. Normalization was done by removing the operator effects from the model fitted data. There was a close correspondence of the model fitted-values to the experimental data, indicating that the model fits the data well (Figure 2). The residuals are approximately normally distributed (Figure E2, Supplementary Materials). There was a strong operator effect in our data set (Figure E3). The normalization (Methods, Eq. 5) using the mixed-effects model (Methods, Eq. 1) removed this random effect.

3.2 Normalized versus Raw Data

The relationship between ligands and phospho-proteins are visualized by cytoscape plots, where the ligands are linked to downstream phospho-proteins on the basis of the mixed-effects coefficients. Inspection of the raw data (Figure E4) shows strong stimulation by multiple ligands on many phospho-proteins. However, the normalized data exhibits stimulation of certain, specific phospho-proteins that we compared with the known information about the effects of these stimulants. In the hSAEC raw data, we see strong associations of the ligands TGFβ, lipopolysaccharide (LPS) and interferon (IFN)β with pGSK3α; menadione (Mena) with pERK1/2 and pHSP27; and TNFα with pATF2 and pHSP27 (Figure E4A). In contrast, after the data is normalized, there is a distinct phospho-protein network representation (Figure 3A). Here, the strong induction of pGSK3α by TGFβ and IFNβ associated with the experiments performed by a single operator (Figure E4) are removed. The strong couplings of Mena and TNFα to pHSP27 are retained.

Analysis of the normalized model shows that TGFβ, Mena and TNFα are the strongest inducers of phospho-protein response in hSAECs (Figure 3A). In particular, among the phospho-proteins we studied, TGFβ is shown to strongly affect pSMAD2 levels (Moustakas *et al*, 2001). TNFα is strongly coupled with pHSP27, and has less strong correlations with pATF2, pCREB and pp65. Mena is strongly coupled to pHSP27, pERK1/2 and pp38MAPK (Figure 3A). The normalized data also correctly shows that IL-6 stimulates pSTAT3 induction. Together we interpret these data to indicate the mixed-effects modeling converges

on a stable prediction, consistent with known signaling pathways and that normalization is essential to remove random effects.

For the EMT-hSAECs, analysis of the predictions from raw data suggests strong inductions by many stimulants, including TGFβ (Figure E4B). However, this conclusion is artificial, as the experimental induction of the EMT state involves prolonged TGFβ exposure, a condition that downregulates the TGFBR, rendering the cell insensitive to subsequent exogenous TGFβ stimulation. Previous work has shown that TGFβ binding promotes TGFBR internalization and degradation [28]. The predictions by the normalized mixed-effects data accurately point to attenuated effects of TGFβ EMT-hSAECs (Figure 3B).

3.3 hSAEC and EMT-hSAEC

We next sought to apply the mixed effects modeling to understand how the topology of ligand-phospho-protein coupling changes as a result of the mesenchymal transition. Overall, we observed that phospho-protein induction is decreased in EMT-hSAECs (Figure 3B). This was corroborated by the mixed-effects model, which calculated the average effect of the EMT state on phosphorylation under all inhibitors/treatments to be −0.52 (in $\log_{10}$). Looking at the terms representing the interaction between the EMT state and each individual phospho-protein, we found 4 proteins - pATF2, pCREB, pERK1/2, and pSMAD2 – that have a positive value, and thus do not exhibit as much of a down-regulation in signaling as the other surveyed phospho-proteins. pHSP27 had the strongest negative interaction value with EMT, which is reflected by the significant decrease in HSP27 phosphorylation in EMT-hSAECs compared to hSAECs (Figure 3). Similarly, Mena retains a strong interaction with pERK1/2 and pp38MAPK, but coupling with pHSP27 is lost. Additionally, there is a loss in IL-6 mediated STAT3 phosphorylation and TGFβ mediated SMAD2 phosphorylation in EMT-hSAECs (Figure 3B).

Transcriptional reprogramming induced by TGFβ stimulation may affect the abundance of the phospho-proteins modeled in our study. We therefore incorporated the results of a quantitative proteomics study analyzing steady state protein differences between hSAECs and EMT using isobaric tags for relative and absolute quantitation (iTRAQ). In this analysis, to be reported in detail elsewhere (Y Zhao, in preparation), the relative abundance of 11 of the 13 phospho-protein substrates were quantified by iTRAQ in hSAECs versus EMT. We observed the abundance of the AKT, SMAD2, CREB, p38MAPK, GSK3, STAT3, ERK1 substrates were within 20% of that in control hSAECs (Figure E4C). By contrast, the abundance of RelA and ATF2 were increased 40% above hSAEC levels, whereas that of P90RSK and Hsp27 were significantly reduced by 25% and 40%, respectively of that in hSAECs (Figure E4C).

To account for the potential impact of the 40% reduction of HSP27 in the EMT state, the ligand effects were corrected for the differences measured in the initial phospho-protein levels. As seen in Figure 3C, correction for the substrate abundance does not affect the overall interpretation of the coupling of the ligand-phospho-protein substrates in EMT. Importantly, correction for HSP27 concentration does not reverse the functional defect in TNF-pHSP27 coupling, nor the defect in Mena-pHSP27 coupling. This abundance information extends our interpretation of the mixed-effects modeling that the reduced

abundance of phospho-proteins in EMT is not simply a consequence of reduced substrate abundance, but rather due to differences in functional coupling of phosphorylation networks.

3.4 Inhibitor Effects

We examined the effects of several inhibitors in this study - iATM, iIKK, iJAK, iMEK, and iSTAT3 (Figure 4). Here normalized phospho-proteins levels at time 0 and 15 min are plotted for each ligand and inhibitor combination by cell state. As a rule, inductions (by the stimulants) of phospho-proteins in EMT-hSAECs treated with inhibitors were markedly weaker than those in hSAECs. Here, again, we observed the agreement between predictions from the mixed-effects model and expected results. For example, in iMEK treated samples, the model shows no stimulation of pERK1/2 under all stimuli (Figure 4 A), which was expected, as MEK is an upstream kinase of ERK1/2 in the MAPK pathway. Strong pSMAD2 induction by TGFβ was observed in hSAECs under all inhibitor conditions. These are similar to the corresponding observations in hSAECs with no inhibitors (Figure 3A). Also unaffected is the TNFα-stimulated induction of NFκB/pp65 (Figure 4A. This induction in hSAECs was retained under all inhibitor conditions, though slightly attenuated in iSTAT3- and iIKK- treated cells. The induction of pHSP27 by TNFα stimulation was strongly attenuated in iMEK- and iSTAT3- treated hSAECs whereas the other inhibitors greatly increased it (Figure 4A). EMT-hSAECs exhibited significant downregulation of pHSP27 under all inhibitor conditions (Figure 4 B).

Induction of pSTAT3 was the primary effect of IL-6 stimulation on hSAECs in our experiments with no inhibitors (Figure 3A). Treatment with iATM, iIKK, and iMEK do not affect pSTAT3 induction by IL-6 (Figure 4A). The results for hSAECs treated with iSTAT3 or iJAK showed small changes in the levels of pSTAT3 (Figure 4A) upon IL-6 stimulation. We observed increased levels of ERK1/2 in iSTAT3-treated cells under IL-6 treatment (Figure 4A). This result suggests that, under IL-6 treatment, when STAT3 protein activity is blocked, alternative cell response pathways are induced via ERK1/2 of the MAPK pathway. The induction of pSTAT3 by IL-6 was lost in EMT-hSAECs under all inhibitor conditions (Figure 4B), suggesting a general defect in the IL-6 signaling pathways following EMT.

3.5 Correlative Network Topology

To determine how mesenchymal transition rewires the phospho-protein networks, we sought to identify which phospho-proteins are co-regulated or respond to the stimuli in a coordinated manner. For this purpose, we calculated the correlations between each pair of phospho-proteins using vectors derived from the normalized data. First, we computed pairwise Pearson correlations between the phospho-proteins and adjusted them for multiple hypothesis testing. There were 18 and 21 highly significant correlations ($p < 0.01$) in the hSAECs and EMT-hSAECs, respectively (Figure E5). All significant correlations were positive, with the average absolute correlations being 0.62 and 0.67 in EMT-hSAECs and hSAECs, respectively. We note that the computed correlations are those between the phospho-proteins in each cell state, separately. They are independent of the change of a protein abundance between the cell states.

In the EMT-hSAECs, we observed markedly decreased levels of pHSP27. We note that this phospho-protein corresponds to the highest singular value [29] in the column space of the data matrix (Methods) for hSAECs. In the EMT-hSAECs, pHSP27 corresponded to the sixth (out of thirteen) most important singular value. The three most important phospho-proteins in the EMT-hSAECs (as computed using the singular value decomposition) with comparable coefficients (0.4, 0.5, and 0.6) were pATF2, pCREB and pERK1/2, respectively (Figure 5A).

The phospho-proteins in our samples are functionally diverse and included kinases, transcription factors and a chaperone protein. It is expected that substrates will correlate with their up-stream kinases. The correlations are reflected in the Pearson's coefficients. However, there existed correlations that were not reflective of the functional alignment of the proteins in a particular signaling pathway. To remove these correlations and refine the network topology, first-order partial correlations were calculated by conditioning the correlations between two proteins on a third protein [26]. The partial correlations can be helpful in uncovering conditional independence of phospho-proteins [13]. For example, the zeroth order correlation (original Pearson's correlation with no conditioning) between pHSP27 and pERK1/2 was statistically highly significant and equal to 0.6 in hSAECs. However, when conditioned on pp38MAPK, the correlation was non-significant and equal to −0.04. Thus, the zeroth order correlation between pHSP27 and pERK1/2 existed due to the correlations between pHSP27 and pp38MAPK, and pERK1/2 and pp38MAPK. When the correlation between pp38MAPK and pHSP27 was conditioned on pERK1/2, it was still highly significant. Another illustrative example involved pERK1/2, pp38MAPK and pp90RSK. The latter two are highly correlated with the zeroth order Pearson’s correlation coefficient of 0.69 (the corresponding p-value is 6.3e-08). However, when this correlation was conditioned on pERK1/2, it dropped to 0.1 and became non-significant. This result is in agreement with the fact that ERK1/2 is an upstream kinase of p90RSK. It is important to note that not all conditionings are meaningful. The conditioning will be the most informative if at least two of the phospho-proteins are on the same signaling pathway.

For our partial correlation analysis, we conditioned the correlation of transcription factors with the other phospho-proteins on the kinases (pp38MAPK, pERK1/2, pp90RSK and pGSK3α) only. We did not include pAKT in the list, as it did not show any significant pairwise correlation in the zeroth order with any of the phospho-proteins. pGSK3α showed highly significant correlations in EMT-hSAECs only, and was used in conditioning of correlations in those cells only. After the partial correlation test, there were 14 and 13 pairwise protein correlations that were statistically highly significant in hSAECs and EMT-hSAECs, respectively (Figure 5B). Several correlations originating from pp38MAPK that were present in hSAECs were absent in the EMT-hSAECs.

However, there emerged new correlative connections involving pSMAD2 and pGSK3α in the EMT-hSAECs. pSMAD2 significantly correlates with pHSP27 and pGSK3α, and pGSK3α significantly correlates with pCREB and pATF2. To determine the reasons for these changes, we examined the correlations for each phospho-protein separately between the two cell states. It turned out that all phospho-proteins, except for pSMAD2 and GSK3α, had statistically significant positive correlations. The correlation coefficients were 0.07 (p-

value 0.64) and 0.27 (p-value 0.05) for SMAD2 and GSK3α, respectively. It means to us that the responses of these phospho-proteins in hSAECs and EMT-hSAECs were different. The association between SMAD2 and GSK3α may be significant, as phosphorylation of the SMAD2 linker domain is controlled by an AKT/GSK3 cross-talk pathway, producing resistance to TGFβ-mediated cell cycle arrest in cancer cells [30].

The design of the experiment allowed pairwise correlations between phospho-proteins in a cell state and between cell states. In addition, it also allowed computing correlations between the stimulants. The two stimulants who caused the most correlated responses were TGFβ and Poly(I:C), with a correlation coefficient was 0.92; all other correlations were smaller. The clustering of the stimulants based on the responses from the 13 phospho-proteins are shown for hSAECs (Figure E6A) and EMT-hSAECs (Figure E6B). In hSAECs, the response patterns produced by TNFα and Mena co-cluster, as do TGFβ and polyIC. There is a change in the clustering of stimulants in hSAECs and EMT-hSAECs. In the ETM-hSAECs, the strongest correlation of TGFβ is with IFNβ.

3.6 Validation of pp38MAPK-independent HSP27 Phosphorylation Loss

In hSAECs, we observed a strong positive correlation between pp38MAPK and pHSP27 (Figure 5B1). However, in the case of the iJAK inhibitor and TNFα stimulation, the model predicts unchanged levels of pp38MAPK and elevated levels of pHSP27. We hypothesized that under this condition, HSP27 was activated by an ancillary pathway independent of pp38MAPK. To test this hypothesis we designed experiments where hSAECs were treated with an inhibitor of p38MAPK, ip38. We expect that the ip38 treatment will not affect the increase in levels of pHSP27. Triplicate measurements were performed on inductions of the phospho-proteins in response to stimulation by TNFα in hSAECs and EMT-hSAECs treated with ip38, iJAK and a combination of the two.

The results demonstrated that pHSP27 is in fact induced (highly significantly) in hSAECs treated with ip38 (Figure 6). Consistent with the model, we also observed statistically non-significant (t-test) changes of pHSP27 in EMT-hSAECs. Induction of pp38MAPK in the hSAECs and EMT-hSAECs treated with ip38 was not statistically significant (t-test). Similar results for iJAK and a combination of iJAK+ip38 treated samples were obtained and are shown in Figures E7 and E8.

3.7 HSP27 effects on STAT3 signaling

One of the canonical connections lost following EMT is that of IL-6 and STAT3. It has been shown that pHSP27 interacts with, and may facilitate phosphorylation of, STAT3 [31]. To determine if the loss of STAT3 signaling was associated with the 40% decrease we observed in pHSP27 due to EMT (Figure E4 B), we overexpressed HSP27 in EMT-hSAECs and subjected the cell populations to flow cytometry analysis gating by pSTAT3 signal (Figure 7). It can be seen from the Figure that IL-6 stimulation induced STAT3 phosphorylation in ~ 97.8% of hSAECs. While with the same gate in IL-6 stimulated EMT-hSAECs, HSP27 overexpression increased the percentage of pSTAT3 positive cells from 23.2% to 36.5%. This data confirms the loss of IL-6 induced pSTAT3 in EMT-hSAECs and further indicates that the overexpression of HSP27 in EMT-hSAECs partially restored STAT3

phosphorylation. It suggested that while the loss of HSP27 can partially account for the decreased levels of pSTAT3, there are still additional defects in the pathway.

4 Discussion

In this study, we characterized some of the changes in network phospho-protein topology following EMT in hSAECs. The removal of the operator effects by normalization using mixed-effects modeling is a necessary step for analyzing ELISA data from multiple experiments. After removal of the random effects, the model correctly predicted known stimulus effects (e.g., TGFβ-induced pSMAD2 inductions, and TNFα-induced NF-κB/pp65 inductions) from the fixed effects. The normalized data showed that the most pronounced changes in signaling following EMT occurred with the application of TNFα and Mena, suggesting a defect in a signaling in a pathway that is shared between the two ligands.

TNFα is a prototypic monokine that binds to ubiquitous death domain-containing receptors, stimulating their membrane aggregation [32]. This d receptor-associated factors (TRAFs) to form a functional submembranous, intracellular signaling complex that stimulates inflammatory responses and activates innate immunity. Mechanisms that mediate the actions of TNFα have been intensively studied [33]. The three major intracellular pathways that are activated by TNFα are caspases, NF-κB, and MAPK. Our analysis is consistent with the activation of NF-κB and MAPK kinase pathways in hSAECs.

The normalized data indicate that TNFα is associated with a strong induction of pHSP27 (Figure 2B). HSP27 is an ATP-independent chaperone important in cytoskeletal organization, which confers protection against apoptosis through various mechanisms, such as a direct interaction with cytochrome c to prevent formation of an apoptosome with Apaf-1 (apototic protease activating factor-1) and caspase-9 [34]. pHSP27 also reduces production of reactive oxygen species (ROS) induced by TNFα by increasing intracellular glutathione levels [35]. In another role, it has been shown that in response to TNFα, HSP27 overexpression in various cell types enhances the degradation of ubiquitinated proteins by the 26S proteasome [36]. It is thought that HSP27 binds to polyubiquitin chains and to the 26S proteasome *in vitro* and *in vivo*. The ubiquitin-proteasome pathway is involved in the activation of transcription factor NF-κB by degrading its main inhibitor, IκBα [37]. pHSP27 does not affect IκBα phosphorylation but enhances the degradation of phosphorylated IκBα by the proteasome [36]. This function of HSP27 accounts for its anti-apoptotic properties through the enhancement of NF-κB activity.

In EMT-hSAECs, the abundance of RelA and ATF2 is increased by 40%, whereas that of p90RSK and HSP27 is reduced by 25% and 40%, respectively. Despite these minor changes, the inclusion of abundance data does not substantially affect the interpretation of our difference analyses (Figures 3A, B and C). In the mesenchymal transition, we observe that TNFα does not induce any HSP27 phosphorylation (Figure 3 C). In fact, it does not strongly induce phosphorylation of any of the phospho-proteins sampled in this study. Previous studies have shown that TNFα induces NF-κB/RelA binding to promoter at similar levels in hSAECs and EMT-hSAECs [10], indicating that this is not a result of internalization of the TNF receptor. We note that this lack of HSP27 induction does not

result in higher levels of apoptosis, as EMT-hSAECs are resistant to apoptosis. The transcription factor SNAI, which is involved in EMT progression, down-regulates many pro-apoptotic genes [38].

Results from hSAECs also predict elevated levels of phospho-Ser536 NF-κB (pp65) upon TNFα stimulation (Figure 3 A). NF-κB/p65 is activated by serine phosphorylation at multiple sites; of these Ser536 phosphorylation is controlled by a diverse set of kinases, including NF-κB inducing kinase , IKKβ, and protein kinase Cζ [39]. This phophorylation is significantly reduced following EMT. Studies in liver myofibroblasts have shown that p-Ser536-p65 is constitutively activated and contributes to myofibroblast survival [40]. Further studies are necessary to determine if this phenomenon occurs in EMT-hSAECs as well.

TNFα activation of MAPK kinase pathways [33] was observed, as seen by the elevated levels of pp38MAPK and pERK1/2 (Figure 2B). The activated MAPKs relocate into nucleus and phosphorylate transcription factors, CREB and ATF2 resulting in the increase of pCREB and pATF2 (Figure 2B). In EMT-hSAECs that were treated with ip38, we see that HSP27 signaling is markedly reduced (Figure 6). This points to a disruption in a p38MAPK-independent pathway that activates HSP27. Alternate pathways for HSP27 phosphorylation at Ser78 include the Protein Kinase A (PKA) pathway [41]. PKA has been implicated in hypoxia-mediated EMT in lung cancer [42].

Mena is a vitamin K-like naphthoquinone derivative. It can under-go two types of biologically relevant reactions: arylation and redox cycling [43]. Arylation results in the activation of tyrosine phosphatases, thus activating the epidermal growth factor receptor (EGFR) signaling pathway. Redox cycling generates ROS, which, at low levels, can trigger signal transduction, but at high levels results in oxidative damage and cell death [44]. Activation of the EGFR pathway results in upregulation of ERK1/2. ROS signaling leads to the activation of p38MAPK [45]. We also see increased phosphorylation of CREB and ATF2, which are downstream targets of these MAPKs (Figures 2 and 3). Mena stimulation also results in a significant increase in pHSP27 (Figure 2), which can act as an anti-oxidant protein, potentially allowing cells to resist the effects of oxidative stress and prevent apoptosis [46]. This may occur via ROS signaling and the p38 MAPK pathway [47].

In EMT-hSAECs, Mena was the only ligand that induced significant phosphorylation in any of the proteins assayed. The upstream EGFR and ROS signaling pathways through MAPKs appear to be intact, as the connections to p38MAPK, ERK1/2, and ATF2 are maintained. We observed a reduction in CREB and HSP27 phosphorylation with both Mena and TNFα, which points to a defect in a CREB/HSP27-related pathway. PKA is an activator of both of these proteins. Further studies on the PKA pathway will reveal if it is indeed disrupted following EMT.

Overall, there was a global reduction in phospho-protein inductions in EMT-hSAECs, particularly for pHSP27. Through the use of appropriate computational methods, we uncovered previously unknown changes that occur in phospho-protein signaling networks due to Type-II EMT. EMT was found to be associated with the loss in couplings of IL-6 to

pSTAT3 and TNFα to pHSP27, indicating profound rewiring of phospho-protein signaling networks and their connections. The correlative study of the phospho-proteins under multiple stimuli and inhibitor conditions revealed that the phospho-proteins in EMT-hSAECs exhibited more couplings, but with smaller coefficients. We observed a new, potentially significant correlation between pSMAD2 and GSK3α. Further studies will uncover the full extent of signaling differences in normal and EMT-transformed cells. These altered networks may represent potential targets for therapeutics that can modulate EMT and restore normal function to transformed cells.

5 Conclusions

We applied the mixed-effects modeling to study the cellular signaling perturbations in hSAECS and EMT-hSAECs. After the removal of the random effects the model correctly predicted known stimulus effects (TGFβ-induced pSMAD2 inductions, and TNFα-induced NFκB/pp65 inductions) from the remaining fixed effects.

We observed a global reduction in phospho-protein inductions in EMT-hSAECs, particular for pHSP27. The EMT was found to be associated with the loss in couplings of IL6 to pSTAT3 and TNFα to pHSP27, indicating that the EMT was accompanied by profound rewiring of phospho-protein signaling networks and their connections. The correlative study of the phospho-proteins under multiple stimuli and inhibitor conditions revealed that the phospho-proteins in EMT-hSAECs exhibited more couplings, but with smaller coefficients. We observed a new, potentially significant correlation between pSMAD2 and GSK3α.

Supplementary Material

Refer to Web version on PubMed Central for supplementary material.

Acknowledgements

We thank Karon Cassidy, M.D., for her critical review of the manuscript. RGS acknowledges support by the National Institute Of General Medical Sciences of the National Institutes of Health under Award Number R01GM112044. This project was supported, in part, by UL1TR000071, the UTMB Clinical and Translational Science Award; HHSN272200800048C, the NIAID Clinical Proteomics Center; NIH-NLBIHHSN268201000037C, the NHLBI Proteomics Center for Airway Inflammation; and NIEHS P30 ES006676 (C. Elferink, PhD). Core laboratory support was from the UTMB Flow Cytometry Core, the Optical Imaging Laboratory, and the SCMM proteomics facility.

Abbreviations

AKT	protein kinase B
ATM	ataxia-telangiectasia mutated
ELISA	enzyme-linked immunosorbent assay
EMT	epithelial-mesenchymal transition
ERK	extracellular signal-regulated kinase
GSK	glycogen synthase kinase

hSAEC	human small airway epithelial cell
HSP	heat shock protein
IGF	Insulin-like growth factor
IκB	inhibitor of NFκB;
IKK	an inhibitor of the IκB-kinase
INF	interferon
JAK	janus kinase
JNK	c-Jun N terminal kinase
LPS	lipopolysaccharide
MEK	mitogen associated kinase
Mena	menadione
MMP	matrix metalloproteinase
PI3K	phosphoinositide 3-kinase
PolyIC	Polyinosinic:polycytidylic acid
SMA	smooth muscle cell actin
SMAD	small body size/ Mothers Against Decapentaplegic
STAT	signal transducers and activators of transcription
TGF	transforming growth factor
TNF	tumor necrosis factor
TRAF	TNF receptor associated factor
ZEB	zinc finger E-box binding

Reference List

1. Knight DA, Holgate ST. The airway epithelium: structural and functional properties in health and disease. Respirology. 2003; 8:432–446. [PubMed: 14708552]
2. Lambrecht BN, Hammad H. The airway epithelium in asthma. Nat.Med. 2012; 18:684–692. [PubMed: 22561832]
3. Ijaz T, Pazdrak K, Kalita M, Konig R, Choudhary S, Tian B, Boldogh I, Brasier AR. Systems biology approaches to understanding Epithelial Mesenchymal Transition (EMT) in mucosal remodeling and signaling in asthma. World Allergy Organ J. 2014; 7:13. [PubMed: 24982697]
4. Holgate ST, Bodey KS, Janezic A, Frew AJ, Kaplan AP, Teran LM. Release of RANTES, MIP-1 alpha, and MCP-1 into asthmatic airways following endobronchial allergen challenge. Am.J.Respir.Crit Care Med. 1997; 156:1377–1383. [PubMed: 9372648]
5. Katsuno Y, Lamouille S, Derynck R. TGF-beta signaling and epithelial-mesenchymal transition in cancer progression. Curr.Opin.Oncol. 2013; 25:76–84. [PubMed: 23197193]
6. Willis BC, Liebler JM, Luby-Phelps K, Nicholson AG, Crandall ED, du Bois RM, Borok Z. Induction of epithelial-mesenchymal transition in alveolar epithelial cells by transforming growth factor-beta1: potential role in idiopathic pulmonary fibrosis. Am.J.Pathol. 2005; 166:1321–1332. [PubMed: 15855634]

7. Lamouille S, Xu J, Derynck R. Molecular mechanisms of epithelial-mesenchymal transition. Nat.Rev.Mol.Cell Biol. 2014; 15:178–196. [PubMed: 24556840]
8. Kalluri R, Weinberg RA. The basics of epithelial-mesenchymal transition. J.Clin.Invest. 2009; 119:1420–1428. [PubMed: 19487818]
9. Kasai H, Allen JT, Mason RM, Kamimura T, Zhang Z. TGF-beta1 induces human alveolar epithelial to mesenchymal cell transition (EMT). Respir.Res. 2005; 6:56. [PubMed: 15946381]
10. Kalita M, Tian B, Gao B, Choudhary S, Wood TG, Carmical JR, Boldogh I, Mitra S, Minna JD, Brasier AR. Systems approaches to modeling chronic mucosal inflammation. Biomed.Res.Int. 2013; 2013:505864. [PubMed: 24228254]
11. Oliver KG, Kettman JR, Fulton RJ. Multiplexed analysis of human cytokines by use of the FlowMetrix system. Clin.Chem. 1998; 44:2057–2060. [PubMed: 9733011]
12. Clarke DC, Morris MK, Lauffenburger DA. Normalization and statistical analysis of multiplexed bead-based immunoassay data using mixed-effects modeling. Mol.Cell Proteomics. 2013; 12:245–262. [PubMed: 23071098]
13. Kim HD, Meyer AS, Wagner JP, Alford SK, Wells A, Gertler FB, Lauffenburger DA. Signaling network state predicts twist-mediated effects on breast cell migration across diverse growth factor contexts. Mol.Cell Proteomics. 2011; 10:M111.
14. Alexopoulos LG, Saez-Rodriguez J, Cosgrove BD, Lauffenburger DA, Sorger PK. Networks inferred from biochemical data reveal profound differences in toll-like receptor and inflammatory signaling between normal and transformed hepatocytes. Mol.Cell Proteomics. 2010; 9:1849–1865. [PubMed: 20460255]
15. Won JH, Goldberger O, Shen-Orr SS, Davis MM, Olshen RA. Significance analysis of xMap cytokine bead arrays. Proc.Natl.Acad.Sci.U.S.A. 2012; 109:2848–2853. [PubMed: 22323610]
16. Ramirez RD, Sheridan S, Girard L, Sato M, Kim Y, Pollack J, Peyton M, Zou Y, Kurie JM, Dimaio JM, Milchgrub S, Smith AL, Souza RF, Gilbey L, Zhang X, Gandia K, Vaughan MB, Wright WE, Gazdar AF, Shay JW, Minna JD. Immortalization of human bronchial epithelial cells in the absence of viral oncoproteins. Cancer Res. 2004; 64:9027–9034. [PubMed: 15604268]
17. Kalita MK, Sargsyan K, Tian B, Paulucci-Holthauzen A, Najm HN, Debusschere BJ, Brasier AR. Sources of cell-to-cell variability in canonical nuclear factor-kappaB (NF-kappaB) signaling pathway inferred from single cell dynamic images. J.Biol.Chem. 2011; 286:37741–37757. [PubMed: 21868381]
18. Burke JR, Pattoli MA, Gregor KR, Brassil PJ, MacMaster JF, McIntyre KW, Yang X, Iotzova VS, Clarke W, Strnad J, Qiu Y, Zusi FC. BMS-345541 is a highly selective inhibitor of I kappa B kinase that binds at an allosteric site of the enzyme and blocks NF-kappa B-dependent transcription in mice. J.Biol.Chem. 2003; 278:1450–1456. [PubMed: 12403772]
19. Barrett SD, Bridges AJ, Dudley DT, Saltiel AR, Fergus JH, Flamme CM, Delaney AM, Kaufman M, LePage S, Leopold WR, Przybranowski SA, Sebolt-Leopold J, Van BK, Doherty AM, Kennedy RM, Marston D, Howard WA Jr, Smith Y, Warmus JS, Tecle H. The discovery of the benzhydroxamate MEK inhibitors CI-1040 and PD 0325901. Bioorg.Med.Chem.Lett. 2008; 18:6501–6504. [PubMed: 18952427]
20. Lau A, Swinbank KM, Ahmed PS, Taylor DL, Jackson SP, Smith GC, O'Connor MJ. Suppression of HIV-1 infection by a small molecule inhibitor of the ATM kinase. Nat.Cell Biol. 2005; 7:493–500. [PubMed: 15834407]
21. Bates D, Mächler M, Bolker B, Walker S. Fitting Linear Mixed-Effects Models using lme4. Ref Type: Computer Program. 2014
22. R Development Core Team R: A Language and Environment for Statistical Computing.
23. Shannon P, Markiel A, Ozier O, Baliga NS, Wang JT, Ramage D, Amin N, Schwikowski B, Ideker T. Cytoscape: a software environment for integrated models of biomolecular interaction networks. Genome Res. 2003; 13:2498–2504. [PubMed: 14597658]
24. Saez-Rodriguez J, Goldsipe A, Muhlich J, Alexopoulos LG, Millard B, Lauffenburger DA, Sorger PK. Flexible informatics for linking experimental data to mathematical models via DataRail. Bioinformatics. 2008; 24:840–847. [PubMed: 18218655]
25. Benjamini Y, Hochberg Y. Controlling the False Discovery Rate: a Practical and Powerful Approach to Multiple Testing. Journal of Royal Statistical Society. 1995; 57:289–300.

26. de la FA, Bing N, Hoeschele I, Mendes P. Discovery of meaningful associations in genomic data using partial correlation coefficients. Bioinformatics. 2004; 20:3565–3574. [PubMed: 15284096]
27. Voss OH, Batra S, Kolattukudy SJ, Gonzalez-Mejia ME, Smith JB, Doseff AI. Binding of caspase-3 prodomain to heat shock protein 27 regulates monocyte apoptosis by inhibiting caspase-3 proteolytic activation. J.Biol.Chem. 2007; 282:25088–25099. [PubMed: 17597071]
28. Bizet AA, Liu K, Tran-Khanh N, Saksena A, Vorstenbosch J, Finnson KW, Buschmann MD, Philip A. The TGF-beta co-receptor, CD109, promotes internalization and degradation of TGF-beta receptors. Biochim.Biophys.Acta. 2011; 1813:742–753. [PubMed: 21295082]
29. Sadygov RG. Use of singular value decomposition analysis to differentiate phosphorylated precursors in strong cation exchange fractions. Electrophoresis. 2014
30. Abushahba W, Olabisi OO, Jeong BS, Boregowda RK, Wen Y, Liu F, Goydos JS, Lasfar A, Cohen-Solal KA. Non-canonical Smads phosphorylation induced by the glutamate release inhibitor, riluzole, through GSK3 activation in melanoma. PLoS.ONE. 2012; 7:e47312. [PubMed: 23077590]
31. Rocchi P, Beraldi E, Ettinger S, Fazli L, Vessella RL, Nelson C, Gleave M. Increased Hsp27 after androgen ablation facilitates androgen-independent progression in prostate cancer via signal transducers and activators of transcription 3-mediated suppression of apoptosis. Cancer Res. 2005; 65:11083–11093. [PubMed: 16322258]
32. Locksley RM, Killeen N, Lenardo MJ. The TNF and TNF receptor superfamilies: integrating mammalian biology. Cell. 2001; 104:487–501. [PubMed: 11239407]
33. Sabio G, Davis RJ. TNF and MAP kinase signalling pathways. Semin.Immunol. 2014; 26:237–245. [PubMed: 24647229]
34. Bruey JM, Ducasse C, Bonniaud P, Ravagnan L, Susin SA, az-Latoud C, Gurbuxani S, Arrigo AP, Kroemer G, Solary E, Garrido C. Hsp27 negatively regulates cell death by interacting with cytochrome c. Nat.Cell Biol. 2000; 2:645–652. [PubMed: 10980706]
35. Mehlen P, Kretz-Remy C, Preville X, Arrigo AP. Human hsp27, Drosophila hsp27 and human alphaB-crystallin expression-mediated increase in glutathione is essential for the protective activity of these proteins against TNFalpha-induced cell death. EMBO J. 1996; 15:2695–2706. [PubMed: 8654367]
36. Parcellier A, Schmitt E, Gurbuxani S, Seigneurin-Berny D, Pance A, Chantome A, Plenchette S, Khochbin S, Solary E, Garrido C. HSP27 is a ubiquitin-binding protein involved in I-kappaBalpha proteasomal degradation. Mol.Cell Biol. 2003; 23:5790–5802. [PubMed: 12897149]
37. Karin M, Ben-Neriah Y. Phosphorylation meets ubiquitination: the control of NF-[kappa]B activity. Annu.Rev.Immunol. 2000; 18:621–663. [PubMed: 10837071]
38. Franco DL, Mainez J, Vega S, Sancho P, Murillo MM, de Frutos CA, Del CG, Lopez-Blau C, Fabregat I, Nieto MA. Snail1 suppresses TGF-beta-induced apoptosis and is sufficient to trigger EMT in hepatocytes. J.Cell Sci. 2010; 123:3467–3477. [PubMed: 20930141]
39. Leitges M, Sanz L, Martin P, Duran A, Braun U, Garcia JF, Camacho F, az-Meco MT, Rennert PD, Moscat J. Targeted disruption of the zetaPKC gene results in the impairment of the NF-kappaB pathway. Mol.Cell. 2001; 8:771–780. [PubMed: 11684013]
40. Oakley F, Teoh V, Ching AS, Bataller R, Colmenero J, Jonsson JR, Eliopoulos AG, Watson MR, Manas D, Mann DA. Angiotensin II activates I kappaB kinase phosphorylation of RelA at Ser 536 to promote myofibroblast survival and liver fibrosis. Gastroenterology. 2009; 136:2334–2344. [PubMed: 19303015]
41. Kostenko S, Johannessen M, Moens U. PKA-induced F-actin rearrangement requires phosphorylation of Hsp27 by the MAPKAP kinase MK5. Cell Signal. 2009; 21:712–718. [PubMed: 19166925]
42. Shaikh D, Zhou Q, Chen T, Ibe JC, Raj JU, Zhou G. cAMP-dependent protein kinase is essential for hypoxia-mediated epithelial-mesenchymal transition, migration, and invasion in lung cancer cells. Cell Signal. 2012; 24:2396–2406. [PubMed: 22954688]
43. Klotz LO, Patak P, le-Agha N, Buchczyk DP, Abdelmohsen K, Gerber PA, von MC, Sies H. 2-Methyl-1,4-naphthoquinone, vitamin K(3), decreases gap-junctional intercellular communication via activation of the epidermal growth factor receptor/extracellular signal-regulated kinase cascade. Cancer Res. 2002; 62:4922–4928. [PubMed: 12208742]

44. Loor G, Kondapalli J, Schriewer JM, Chandel NS, Vanden Hoek TL, Schumacker PT. Menadione triggers cell death through ROS-dependent mechanisms involving PARP activation without requiring apoptosis. Free Radic.Biol.Med. 2010; 49:1925–1936. [PubMed: 20937380]

45. Chowdhury R, Chowdhury S, Roychoudhury P, Mandal C, Chaudhuri K. Arsenic induced apoptosis in malignant melanoma cells is enhanced by menadione through ROS generation, p38 signaling and p53 activation. Apoptosis. 2009; 14:108–123. [PubMed: 19082730]

46. Paul C, Arrigo AP. Comparison of the protective activities generated by two survival proteins: Bcl-2 and Hsp27 in L929 murine fibroblasts exposed to menadione or staurosporine. Exp.Gerontol. 2000; 35:757–766. [PubMed: 11053666]

47. Huot J, Houle F, Spitz DR, Landry J. HSP27 phosphorylation-mediated resistance against actin fragmentation and cell death induced by oxidative stress. Cancer Res. 1996; 56:273–279. [PubMed: 8542580]

Highlights

- we use mixed-effects modeling phospho-protein to study changes in phospho-protein network topology in EMT
- we use partial correlations to build the phospho-protein networks
- The EMT was associated with the loss in couplings of IL6 to STAT3 and TNFα to HSP27
- EMT rewires p38MAPK-independent HSP27 phosphorylation
- EMT results in an increased correlation between SMAD2 and GSK3 α.

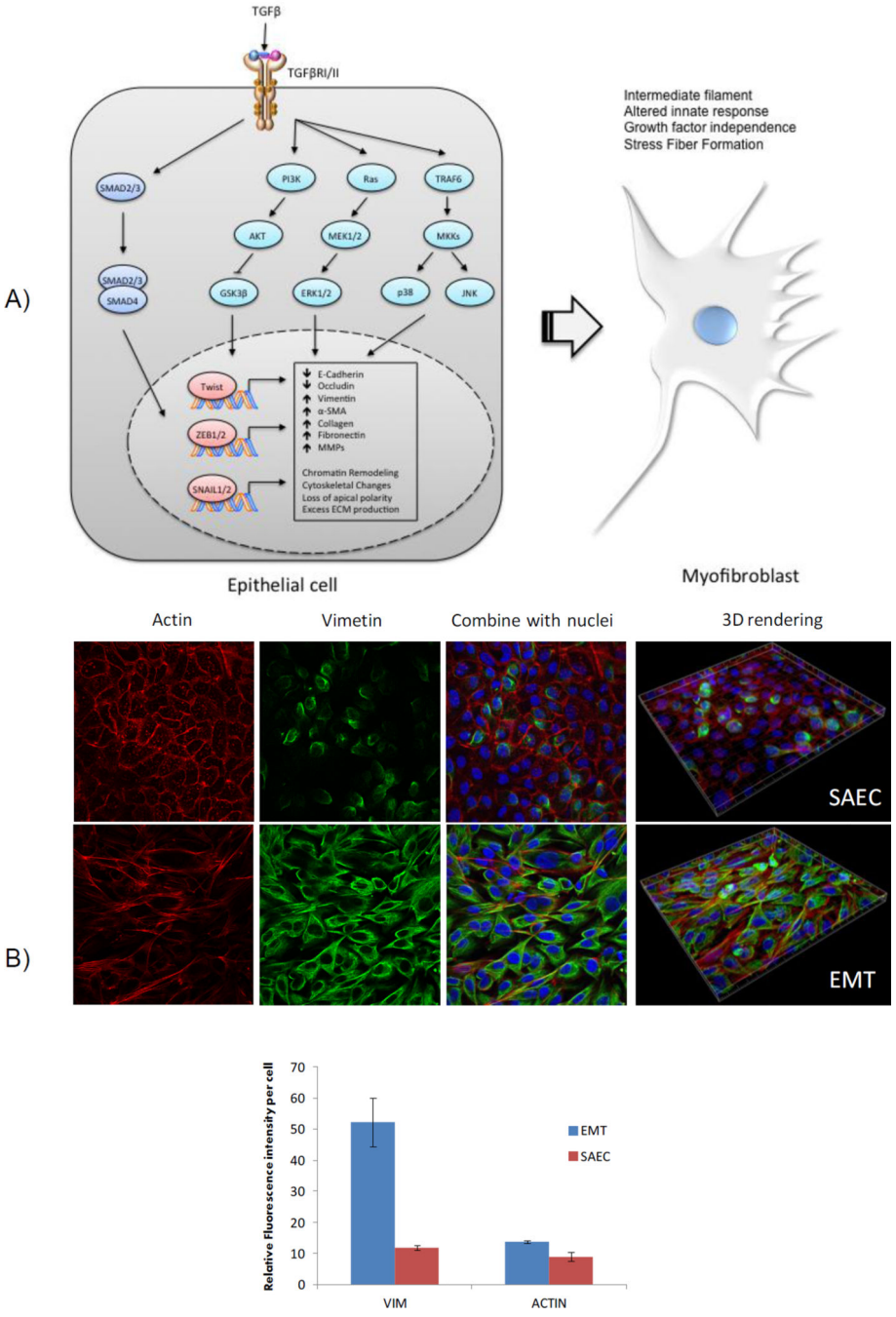

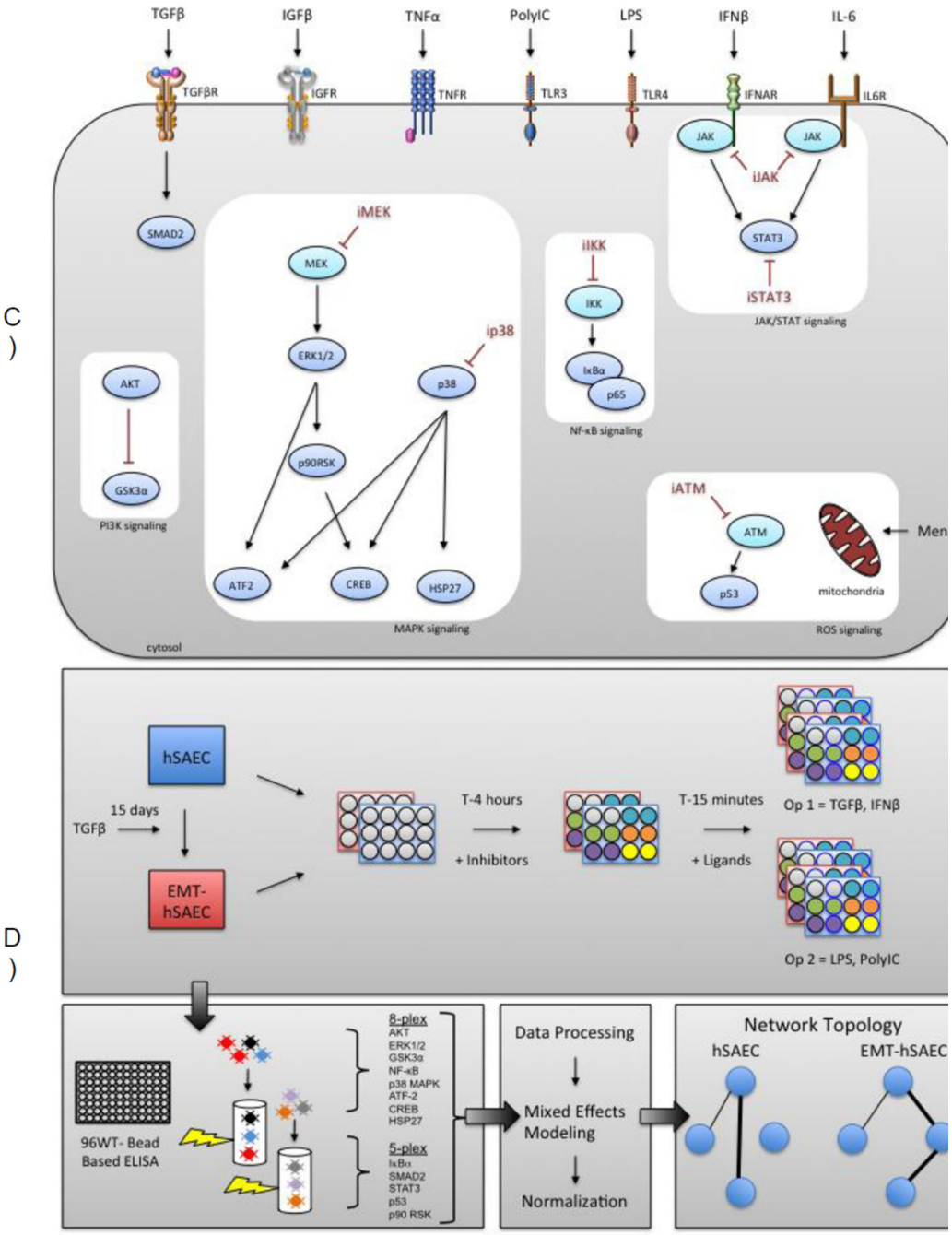

Figure 1. Overview of EMT and Experimental Design

A Mechanism of TGFβ-induced EMT. Epithelial cell stimulation by TGFβ activates the TGFBR canonical SMAD2 (dark blue) and noncanonical AKT/ERK/p38MAPK (light blue) signaling pathways, which converge on the SNAIL, Zinc finger E-box-binding homeobox (ZEB), and Twist transcription factors, causing the cell to adopt a mesenchymal phenotype. **B Phenotyptic changes induced by EMT**. Confocal microscopy of hSAEC (top) and EMT-hSAECs (bottom). The 3 first images on left show a single plane from a z-stack of confocal images taken with 63× 1.2NA objective. The right panel shows the 3D rendering for the

three dimensional reconstruction (z-stack). Pseudocolors were attributed for every chanel. Red: Actin; Green: Vimetin; Blue: nuclei. Relative total cell fluorescence intensity was calculated for the entire cell volume using Metamorph software in 3 different areas. The total fluorescence was then normalized by the number of nuclei yielding the relative fluorescence intensity per cell in both actin and vimetin channels.

C Ligands used and signaling networks targeted in phospho-protein ELISA experiment. A generalized view of the canonical pathways, connections, and proteins involved in this experiment. They cover a variety of pathways, including some that are involved in EMT progression. Measured phospho-proteins are in dark blue, while phospho-proteins that were inhibited but not measured are in light blue. Abbreviations include: TNFα, tumor necrosis factor; IGFβ, Insulin-like Growth Factor β; IFNB, Interferon β; IL-6, Interleukin 6; Mena, menadione; LPS, E. coli lipopolysaccharide; poly(I:C), Polyinosinic:polycytidylic acid.

D Experiment Workflow. An overview of the experimental design and analysis steps. hSAECs and EMT-hSAECs are subjected to treatments of various inhibitors and ligands by different operators and phospho-protein levels are done via ELISA. Following this, data analysis and normalization was done to yield network topology information.

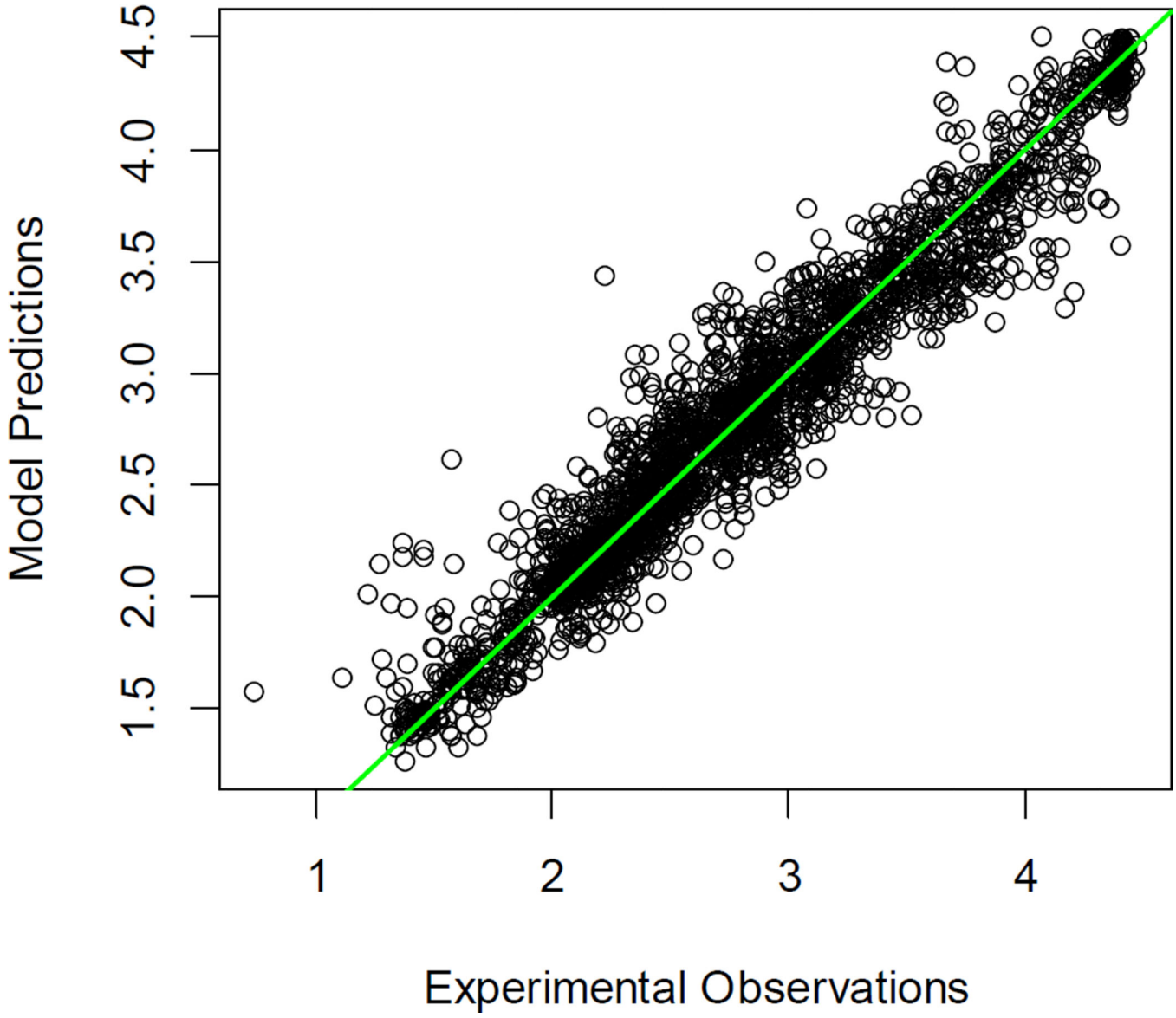

Figure 2. Scatter plot of the model fits (model predictions) and data (experimental observations)

The close correspondence between the model and experimental data indicates that the model fits the data well. The green line depicts the regression line.

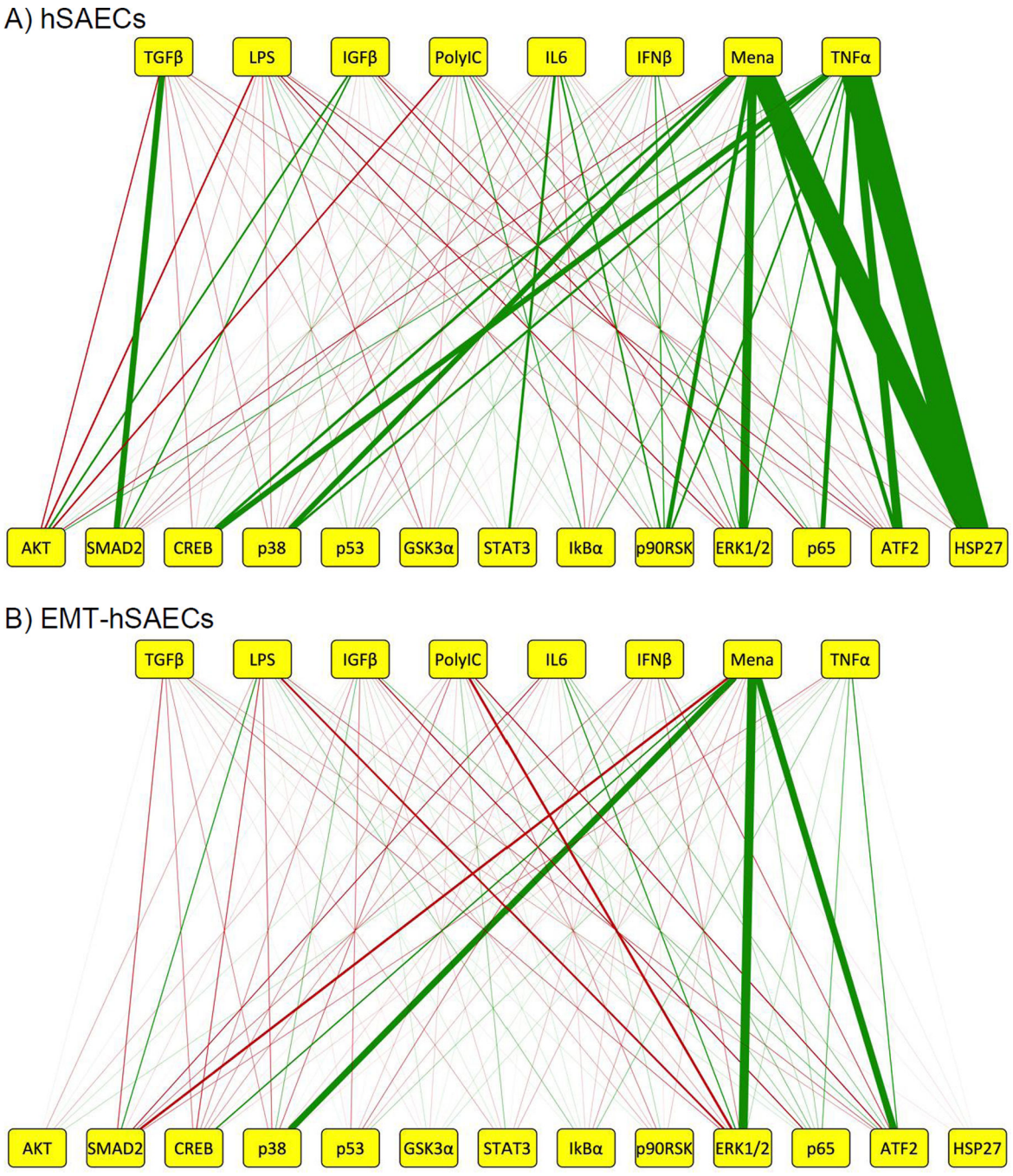

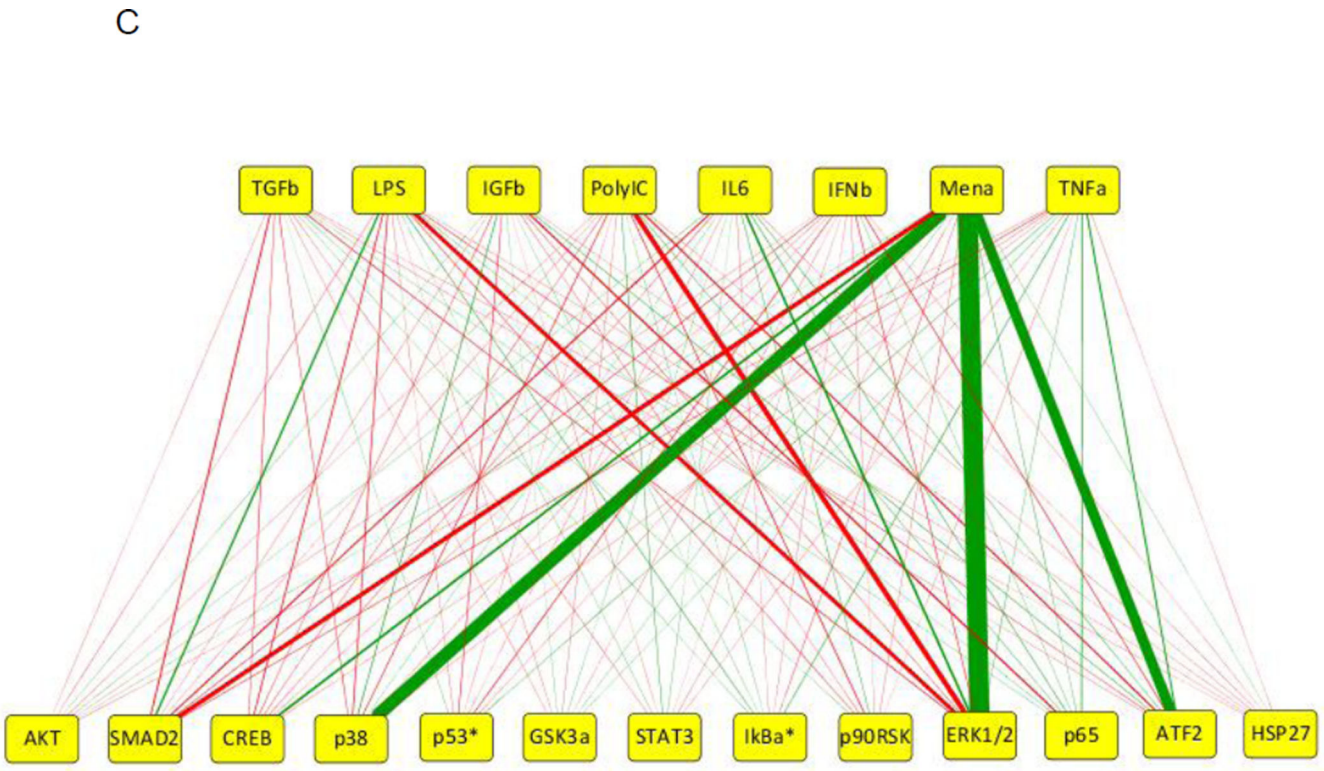

Figure 3. The effects of stimuli on cells with no inhibitor following normalization

Line width corresponds to the difference between phospho-protein level at t=0 and t=15, with green lines representing an increase in phospho-protein levels, and red lines representing a decrease in phospho-protein levels.

A hSAECs. A cytoscape representation of the differences between ligand and phospho-protein in hSAECs.

B EMT-hSAECs. Cytoscape representation of the differences between ligand and phospho-protein in EMT-hSAECs.

C EMT-hSAECs after correction for initial substrate abundance. The edges in Figure 3 B were corrected for the effect of EMT on substrate abundance. A scaling factor was calculated for each substrate based on the ratio of its abundance in control *vs* the EMT state, and used to multiply the difference value for each edge.

*Because p53 and IκBα were not quantified in the iTRAQ analysis, their edges are the same as in Figure 3 B.

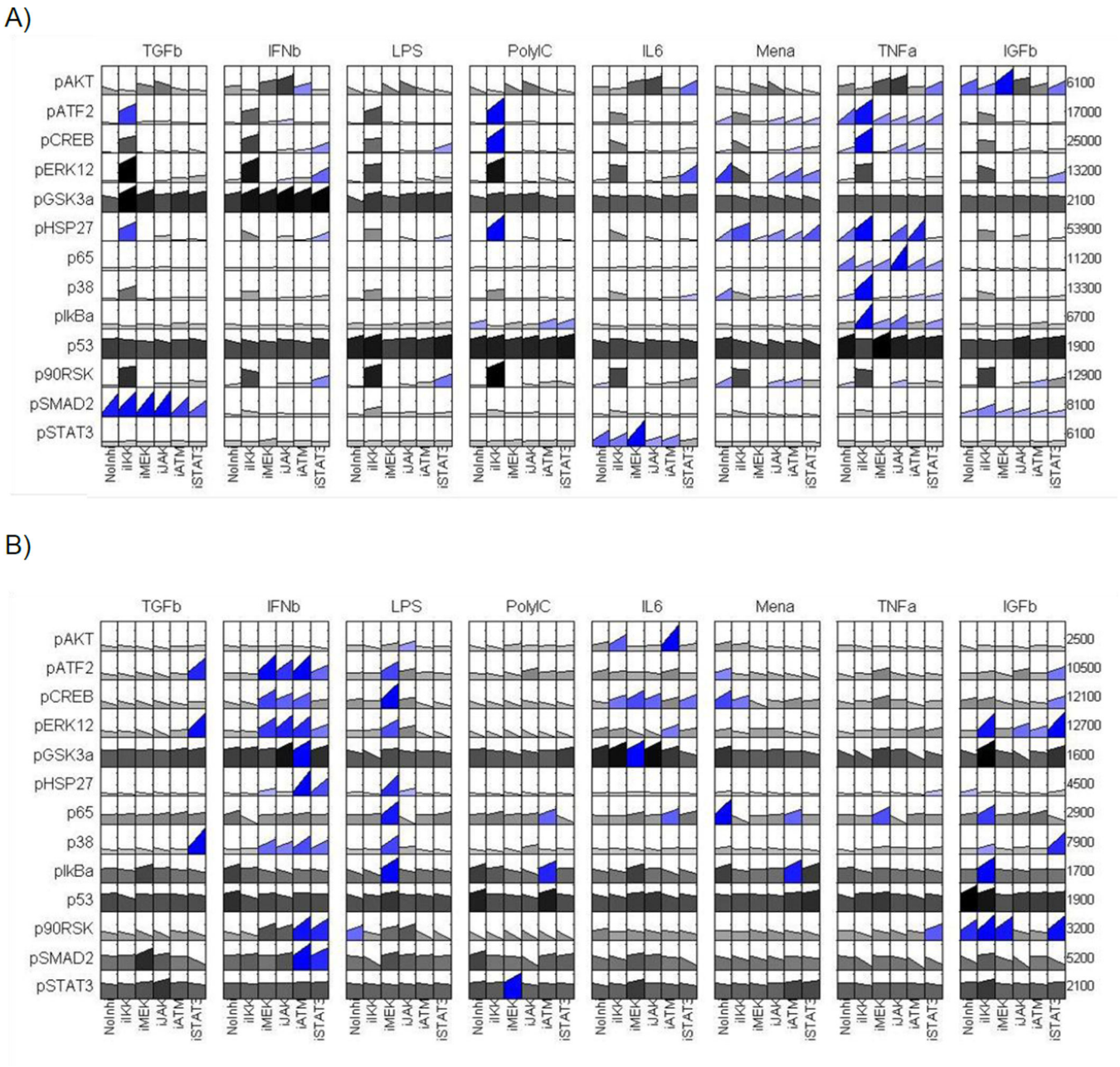

Figure 4. Phospho-protein induction for cells treated with inhibitors (normalized data) ploted using DataRail

A) hSAECs, B) EMT-hSAECs. The blue color denotes significant changes (as determined by DataRail), and grey color indicates non-significant changes.

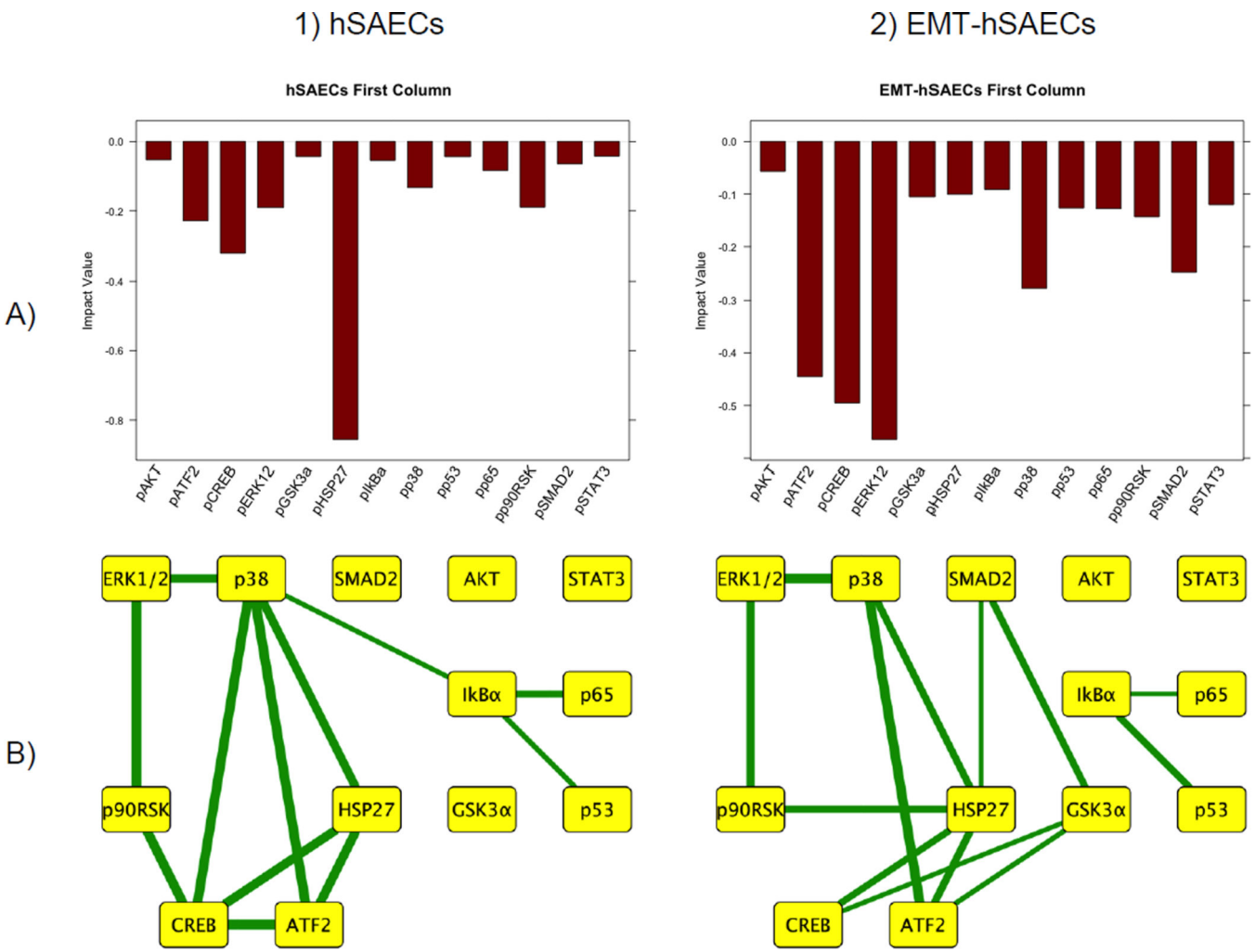

Figure 5. Changes in network topology following EMT

A Singular Value Decomposition. The results from the first column are graphed to show the significant change between states. pHSP27 goes from being the most important value in hSAECs to being relatively unimportant. pATF2, pCREB, and pERK1/2 are the most important phospho-proteins in the EMT state.

B Significant first-order correlations between phospho-proteins. Correlation of the phospho-proteins under all conditions that the cells were subjected to in our study (54 overall). The correlations have been filtered to keep only those with p values < 0.01. The thickness of a line represents the strength of the corresponding correlation.

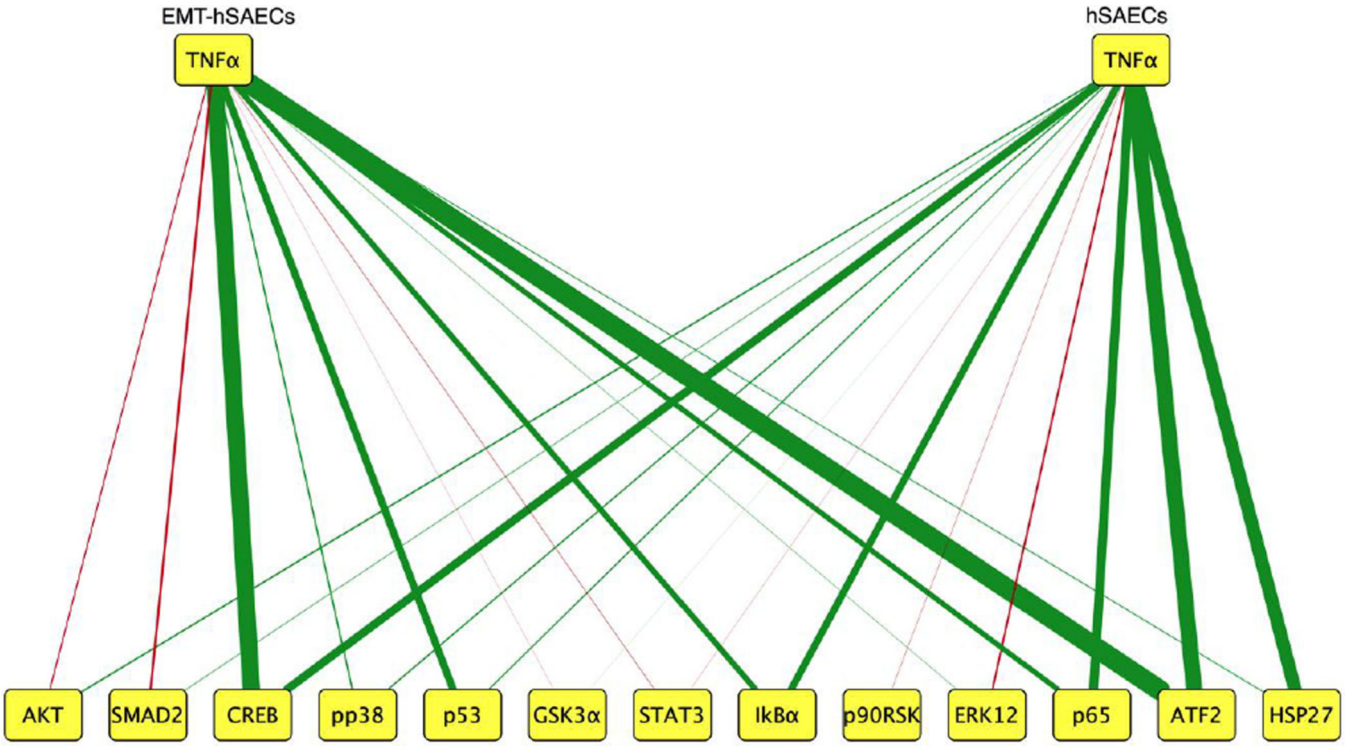

Figure 6. Validating predictions from the mixed-effects model

Phospho-protein inductions in hSAECs and EMT-hSAECs treated with the p38MAPK inhibitor prior to TNFα stimulation. As predicted, we observed a strong induction of pHSP27 in hSAECs while levels of pp38MAPK did not change significantly, along with a significant loss of pHSP27 in EMT-hSAECs. The results are from triplicate measurements.

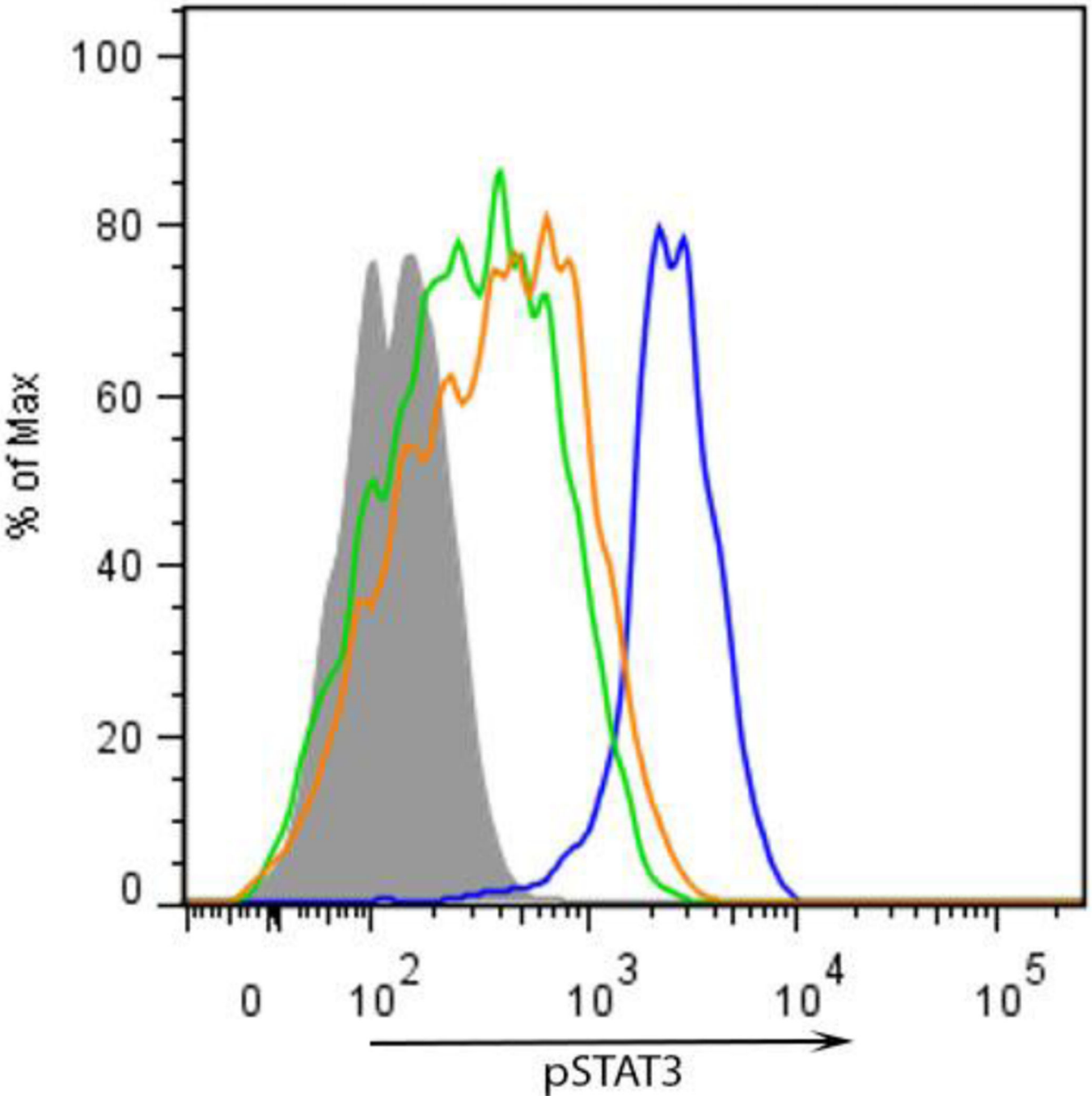

Figure 7. Flow Cytometry shows that HSP27 overexpression in EMT-hSAECs partially restores STAT3 signaling

The hSAECs or EMT-hSAECs transfected by empty vector or HSP27 plasmid were left untreated or IL-6 (100ng/ml) stimulated for 15 min. The pStat3 signal was analyzed by flow cytometry after staining with Alexa Fluro 647 conjugated anti-phospho-STAT3 (Tyr705) antibody. Events were plotted as a function of fluorescence intensity (x-axis). The shaded histogram represents untreated hSAECs, while open histograms represent IL-6 stimulated

cells, either hSAECs (blue curve), empty vector transfected EMT-hSAECs (green curve) or HSP27 transfected EMT-hSAECS (orange curve).